Research paper

A detailed kinetics model for the decomposition of aqueous hydroxylammonium nitrate

Yu-ichiro Izato*†, Kento Shiota**, and Atsumi Miyake**

*Graduate School of Environment and Information Sciences, Yokohama National University, 79−7 Tokiwadai, Hodogaya-ku, Yokohama-shi, Kanagawa, 240−8501 JAPAN
Phone: +81−45−339−3992
†Corresponding author: izato-yuichiro-tk@ynu.ac.jp

**Institute of Advanced Sciences, Yokohama National University, 79−7 Tokiwadai, Hodogaya-ku, Yokohama-shi, Kanagawa, 240−8501 JAPAN

Received: January 10, 2019 Accepted: September 19, 2019

Abstract

Hydroxylammonium nitrate (HAN; [NH_3OH^+] [NO_3^-]) is currently the most promising oxidizer for use in future green liquid propellants for spacecraft applications. To allow the effective development and use of HAN-based propellants, it is important to understand the associated reaction mechanisms, including auto-catalytic processes. The present work developed a detailed chemical kinetics model for the liquid phase reactions of aqueous HAN, based on quantum chemistry calculations using the G4//ωB97X-D/SMD method. The thermal corrections, formation enthalpies, entropies and heat capacities of chemical species were calculated from the partition functions using statistical machinery based on the G4 level of theory. Rate coefficients were also determined to allow the application of transition state theory and variational transition state theory to reactions identified in our previous studies. Thermal and evolved gas analyzes were also conducted for 92 wt% aqueous HAN solution under specific heating conditions. The new model employed herein simulates the thermal decomposition of such a solution, and successfully predicts the heat of reaction and the gases that result from decomposition under these conditions. This new kinetics model also provides a mechanism for the decomposition of HAN. In this mechanism, the initial reaction HAN → HNO+HONO+H_2O triggers the overall decomposition, while the subsequent reactions HAN+HONO → N_2O+2H_2O+HNO_3 and 2HNO → N_2O+H_2O are exothermic and accelerate the decomposition. This mechanism can be summarized by the one-step reaction HAN → 0.75 N_2O+1.75 H_2O+0.5 HNO_3.

Keywords: hydroxylammonium nitrate, liquid phase reaction, detailed kinetic model

1. Introduction

Hydroxylammonium nitrate (HAN)-based liquid propellants such as SHP163[1)−5)] and AF-M315E[6)] are among the most promising candidates as replacements for commonly used mono-propellants such as hydrazine[1)−6)]. However, previous studies have shown that some HAN solutions exhibit extremely high burning rates, and this behavior has limited the potential applications of such propellants[1)−5)], since elevated burning rates can lead to serious accidents[7)−9)]. Therefore, the safe use of HAN-based propellants will require advanced combustion control techniques and an appropriate understanding of the combustion behavior of this compound.

A detailed chemical kinetics model is helpful when investigating rapid transient phenomena such as ignition and extinction in propulsion systems. A sophisticated kinetics model incorporating elementary reactions and all associated chemical species can assist in predicting temporal changes in combustion characteristics, including reactant concentrations, products, temperatures, pressures and the rate determining step. Such models may also provide an improved understanding of the key factors governing various transient phenomena. Many researchers have developed such models, and data is

available for both gas and liquid phase reactions associated with various propellant formulations[10)–19)].

There have been many experimental and theoretical studies aimed at determining the reaction mechanisms associated with HAN combustion, as well as kinetics models. Lee and Litzinger[20)] developed a semi-detailed kinetics model consisting of eight reactions, based on previously proposed reaction mechanisms[21), 22)]. Khare et al.[23)] studied the ignition behavior of HAN/water solutions and developed a theoretical model incorporating earlier gas phase[23), 24)] and condensed phase reaction models reported by Lee and Litzinger[20)]. Ignition delays were calculated using this same approach and the adequacy of electrolytically-induced ignition systems for HAN-based propellants was assessed[23)]. Thynell et al.[25)] developed a detailed kinetics model based on quantum mechanical calculations using the ωB97X-D/SMD method. This model was employed to predict the evolution of various species during the combustion of a 0.1 M HAN solution over the temperature range of 463–523 K, and auto-catalytic mechanisms were discussed. These previous models provide accurate predictions in some cases, but could still be improved by incorporating additional elementary reactions and by evaluating the temperature independence of kinetics and thermodynamic data.

The purpose of the present work was to obtain fully understanding of thermal decomposition of HAN. To this end, we developed a detailed chemical model based on available kinetics data and incorporating reactions identified in our prior quantum chemistry studies[26)–29)], validate this new model by comparison with results obtained from experimental thermal analysis and evolved gas analysis, and proposed a theoretical mechanism for the decomposition of aqueous HAN.

2. Computational and experimental methods

2.1 Quantum chemistry calculations

To identify the reaction mechanisms associated with HAN, we conducted quantum chemistry calculations. Various mechanisms were identified in our previous work[26)–29)] based on the CBS-QB3//ωB97X-D/IEFPCM method, but in the present study we recalculated these processes using the G4//ωB97X-D/SMD method, which may provide more accurate kinetics and thermodynamics.

The geometries and frequencies of the reactants, products and transition states (TSs) were optimized at the ωB97X-D[30)]/6-311++G(d,p) level of theory using the Gaussian 09 program package[31)]. The ωB97X-D method includes empirical dispersion forces and is believed to be reliable when applied to systems with weak van der Waals forces, and yields satisfactory accuracy for kinetics and non-covalent interactions. During computations, TSs were extensively searched for and, if found, an intrinsic reaction coordinate (IRC) calculation was conducted in order to assign reactants and products to the TS. The potential energies of the corresponding molecules were evaluated at the G4 level of theory[32)]. In the original G4 method, the series of calculations starts with geometry optimization at the B3LYP/6-31G (2df, p) level with the zero-point energy scaling factor of 0.9854, followed by a frequency calculation to obtain thermal corrections, zero-point vibrational energy and entropic information. CCSD(T) calculations are subsequently performed with a moderately sized basis set, as are MP4 calculations with a relatively large basis set. Finally, the results of the calculations are combined using an extrapolation scheme, also including zero-point vibrational energy corrections, to approximate the energies that would require more expensive calculations. In the G4//ωB97X-D method employed herein, The optimized geometries based on the ωB97X-D method were fixed with no changes allowed, and the potential energy obtained from the G4 level of theory was corrected using the zero-point energy (ZPE) calculated at the ωB97X-D/6-311++G(d,p) method.

Solvent effects were included by applying the self-consistent reaction field (SCRF) and solvation model based on density (SMD)[33)] options within the program when investigating the liquid reactions. The SMD model is known to generate solvation energies that are typically accurate within 1 kcal mol^{-1} in the case of neutral molecules.

2.2 Kinetics modeling

Rate coefficients for reactions investigated in this study were assessed based on the traditional transition state theory (TST). The rate coefficient, k_{TST}, for the generic reaction A+B → P (where P is one or more products in solution) can be calculated on the basis of TST using the formula

$$k_{TST} = \frac{k_B T}{h} \frac{Q_{TS}}{\prod Q_{reac}} \exp\left(\frac{-\Delta E_0}{RT}\right) \quad (1)$$

where k_B is the Boltzmann constant, T is the temperature, h is the Planck constant, Q_i is the partition function of the reactant or TS, ΔE_0 is the energy barrier to activation and R is the universal gas constant. The value of ΔE_0 in Equation (1) was obtained based on the G4//ωB97X-D/SMD method, while Q values were calculated using the ωB97X-D/SMD method. Variational transition state theory (VTST) was applied to the analysis of dissociation reactions without activation energy barriers. These calculations were performed using the GPOP software package developed by Miyoshi[34)]. The resulting rate coefficients were fit to the modified Arrhenius equation

$$k\ (T) = A \cdot T^n \exp\left(\frac{-E_a}{RT}\right) \quad (2)$$

where k is the rate coefficient, A is a pre-exponential factor, and E_a is the activation energy. It is typically necessary to consider the effect of pressure on the rate of a gas phase monomolecular reaction. However, in the liquid phase, the reactive compound is surrounded by many molecules, and so the liquid state can be considered as equivalent to high pressure conditions. Thus, the rate at the high-pressure limit was used for monomolecular reactions in the liquid phase. Both free radical recombinations and proton transfers with no energy barriers were simply modeled as diffusion-limited

reactions with a rate coefficient of 10^{12} cm^3 mol^{-1} s^{-1}. This assumption is supported by data from the aqueous kinetics database generated by the Notre Dame Radiation Laboratory, which generally shows rate coefficients between 10^{12} and 10^{13} cm^3 mol^{-1} s^{-1} for radical recombination reactions. The diffusivity-dependent encounter rate of two species and the Stokes-Einstein diffusion within the solvent were used to estimate these rate coefficients[14), 35)]. Reactions assessed in this study were abstracted from our previous identification studies[26)–29)].

2.3 Thermodynamic data modeling

Thermodynamic data for all species investigated in this study were also obtained via quantum chemistry calculations using the Gaussian 09 program package[32)], in conjunction with optimization and frequency analysis employing the G4 method[32)]. Solvent effects were included by applying both the SCRF and SMD[33)] options within the program when investigating liquid species.

The heats of formation for gas-phase molecules ($\Delta_f H^\circ_{gas}$) were calculated by the traditional atomization method[36)], and the procedure for a generic molecule ($H_xN_yO_z$) is summarized here. Initially, the atomization energy at 0 K, $\sum D_0(H_xN_yO_z,0K)$, was calculated according to the formula

$$\sum D_0(H_xN_yO_z,0\,K) = xE_0(\mathrm{calc,H}) + yE_0(\mathrm{calc,N}) + zE_0(\mathrm{calc,O}) - E_0(\mathrm{calc},H_xN_yO_z), \quad (3)$$

where E_0 is the total electron energy corrected for the ZPE at 0 K. Subsequently, the enthalpy of formation of the molecule at 0 K, $\Delta_f H(H_xN_yO_z,0\,K)$, was obtained by subtracting $\sum D_0(H_xN_yO_z,0\,K)$ from the sum of the enthalpies of formation of the constituent atoms at 0 K, which have previously been determined experimentally and reported in the literature[36)], as in the Equation (4).

$$\Delta_f H(H_xN_yO_z,0\,K) = x\Delta_f H(H,0\,K) + y\Delta_f H(N,0\,K) + z\Delta_f H(O,0\,K) - \sum D_0(H_xN_yO_z,0\,K) \quad (4)$$

Finally, the standard enthalpy of formation of $H_xN_yO_z$, $\Delta_f H^\circ$, was obtained by correcting for temperature effects, using the Equation (5).

$$\Delta_f H^\circ_{gas} = \Delta_f H(H_xN_yO_z,0\,K) + T_c(H_xN_yO_z) - (xT_c(H) + yT_c(N) + zT_c(O)) \quad (5)$$

where $T_c(H_xN_yO_z)$ is the difference between the enthalpy values at 0 and 298 K as determined by quantum chemistry calculations, and the empirical T_c (atom) values are taken from the literature[36)].

The standard heat of formation for each compound in solution was obtained from the gas phase heat of formation and the enthalpy of solvation at 298.15 K, as in the Equation (6).

$$\Delta_f H^\circ_{aq} = \Delta_f H^\circ_{gas} + \Delta_{solv} H^\circ \quad (6)$$

and

$$\Delta_{solv} H^\circ = H_{liq,calc} - H_{gas,calc} \quad (7)$$

Here, $\Delta_{solv}H^\circ$ is the enthalpy of solvation, while $H_{liq,calc}$ and $H_{gas,calc}$ are the heats of formation at 298.15 K, calculated directly using the G4 method.

Thermal corrections, entropy (S_{liq}) and heat capacity (C_P) values were calculated from the partition function using statistical mechanics, employing the GPOP software[34)]. The experimental values for protons assume $\Delta_f H^\circ(H^+) = 0$. Thus, the estimated absolute value for $\Delta_f H^\circ$ (H^+) must be added to $\Delta_f H^\circ$ (anions) or subtracted from $\Delta_f H^\circ$ (cations) for the experimental heats of formation. The $\Delta_f H^\circ$ (H^+) of 386.3 kJ mol^{-1} [37)] was used in this study.

2.4 Detailed reaction simulations

The YNU-L 3.0 model was developed in the present work, comprising various kinetics parameters (a total of 167 reactions) as well as thermodynamic data for 63 species. These thermochemical data were implemented in the mechanism using the NASA formalism[38)]. To better understand the reactions of HAN in water, the YNU-L 3.0 model was employed to predict the decomposition of a 92 wt% aqueous HAN solution (with water accounting for the remaining 8 wt %) in an adiabatic reactor at constant enthalpy and volume. These calculations were performed with the CHEMKIN-PRO software package[39)], setting the initial density to 1.6 g cm^{-3}, which is a reasonable value for a highly concentrated aqueous HAN solution[40)]. The decomposition reactions were simulated at a heating rate of 1 °C min^{-1} from 50 to 200 °C.

2.5 Experimental

A 92 wt% aqueous HAN solution was obtained from the Hosoya Pyro-Engineering Co., Ltd., Japan, and was used as -received without further purification.

2.5.1 Thermal analysis

Thermal analysis of the HAN solution was performed using a Setaram C80 instrument, so as to acquire data to validate the detailed kinetics model. The apparatus incorporated a Calvet type heat flux calorimeter that allowed accurate and reproducible calorimetric measurements with a sensitivity of 5–10 μW. In each trial, an approximately 20 mg sample was placed in a glass vessel within a high-pressure stainless-steel chamber, after which the chamber with purged with Ar and sealed. The inert inner vessel prevented the specimen from touching the steel walls of the test chamber, which may otherwise have affected the reactivity of the sample. Due to applicable of the inner vessel, the C80 has advantage compared to other instruments. The C80 was calibrated based on assessing the melting behavior of high-purity indium (99.99%). Each specimen was heated from 40 to 200 °C at 1 °C min^{-1}.

2.5.2 Thermal and evolved gas analysis

A thermogravimetry-differential thermal analysis instrument (TG-DTA; Rigaku TG8120) interfaced with a mass spectrometer (MS; Shimadzu QP-2010) was employed during non-isothermal outgassing studies. In this apparatus, the TG-DTA instrument was connected to

the MS via a stainless transfer tube heated to 200 °C, and a He flow through the TG-DTA instrument carried evolved gases to the MS. Both TG-DTA and MS data were acquired simultaneously to determine the thermal behavior of the aqueous HAN and identify the gases evolved upon heating. In each trial, an approximately 3.5 mg sample was placed in an aluminum pan with a pinhole, and was heated from 40 to 200 °C at a heating rate of 10 °C min^{-1} under a continuous purge with a 200 mL min^{-1} He flow. In this study, we attempted to reduce the impact of evaporation with use of pinhole rid. The samples, including aqueous HAN, that have high vapor-pressure may decompose and evaporate simultaneously. A crucible with pinhole may inhibit inner specimens to evaporate because partial pressure of specimens is large comparing with no-rid conditions. The MS was operated in the electron ionization (EI) mode (70 eV), with selected ion monitoring for m/z values of 16, 17, 18, 28, 30, 31, 33, 44, 46, 47, 63 and 96. After each trial, the sample pan was replaced, and a new pan was prepared for next test.

3. Results and discussion

The YNU-L 3.0 model was developed in the present work, comprising various kinetics parameters (a total of 167 reactions) as well as thermodynamic data for 63 species. Table 1 lists the important reactions modeled in this study along with the associated kinetics parameters. Tables 2 provides the heats of formation for gas and liquid phase compounds obtained from the G4 level of theory and thermodynamic data.

To validate the YNU-L 3.0 model, the simulated heat flow curve was compared with the C80 results obtained using a sealed chamber with an inner glass vessel, as shown in Figure 1. The C80 data demonstrate that the onset of thermal decomposition occurred at a $T_{onset,C80}$ value of approximately 149 °C, based on the intersection of the tangent to the peak with the extrapolated baseline, while the exotherm peak appeared at a $T_{top,C80}$ value of approximately 151 °C. The heat of reaction was determined to be 1.6 kJ g^{-1}.

The simulated heat flow curve in Figure 1 was calculated by temporal subtraction of the mixture enthalpy values obtained using the CHEMKIN-PRO software. The simulated $T_{onset,sim.}$ value was 151 °C, while the $T_{top,sim.}$ value was 157 °C. The associated heat of reaction was calculated to be 1.5 kJ g^{-1}, which was in good agreement with that obtained from the C80. Thus, the simulated and experimental thermal properties were consistent with one another.

The simulated outputs of various gases with increasing temperature at a heating rate of 1 °C min^{-1} are presented in Figure 2. At the initial temperature of 50 °C, the ion pair complex ([NH_3OH^+] [NO_3^-]), the dissociated ions (NH_3OH^+ and NO_3^-) and a minor amount of the base and acid forms (HNO_3 and NH_2OH) were all present in chemical equilibrium in the aqueous HAN. The sum of the moles of [NH_3OH^+] [NO_3^-], NH_3OH^+ and NH_2OH, which indicate the unreacted moles (HAN_{total}) is also plotted in Figure 2. This value began to decrease at approximately 151 °C, which is the onset temperature for the exothermic reaction.

Figure 2 also demonstrates that the outputs of the major products H_2O, N_2O and HNO_3 (NO_3^- and H_3O^+) began to increase at 157 °C. Based on the molar ratios of these products, the overall reaction can roughly be summarized as HAN → 0.75 N_2O+1.75 H_2O+0.5 HNO_3.

The gaseous decomposition products generated by the HAN were also investigated using TG-DTA-MS, and Figure 3 summarizes the results. During the thermal decomposition of the aqueous HAN, an endothermic reaction was observed. The endothermic peak and accompanying mass loss and gas evolution are attributed to the decomposition of HAN as well as to the evaporation of both water and HAN. The MS analysis of the evolved gases found peaks at m/z values of 16 (NH_2^+ or O_2^+), 17 (NH_3^+ or OH^+), 18 (H_2O^+), 28 (N_2^+), 30 (NO^+), 44 (N_2O^+), 46

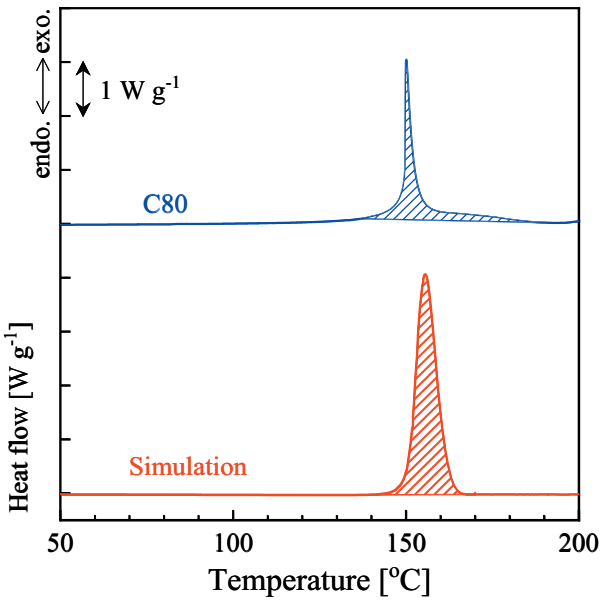

Figure 1 Heat flow curves obtained from C80 measurements and from simulations using the YNU-L 3.0 model.

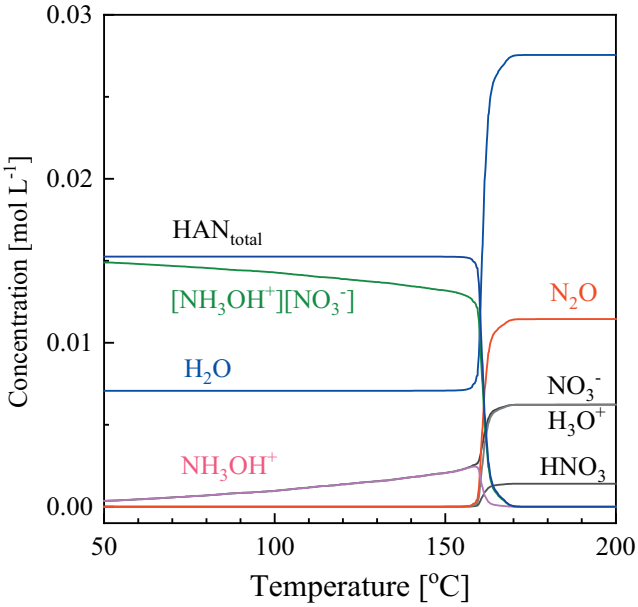

Figure 2 Simulated variations in the aqueous HAN decomposition species with temperature at a heating rate of 1 °C min^{-1}.

Table 1 Reactions and associated rate coefficients employed during the kinetic modeling of radical decomposition. A are given in units of [cm^3], [mol], and [s] ; and E_a is in units of [cal mol^{-1}].

No.	Reactions	k		
		A	n	ΔE_a
R1	HAN → $NH_2OH+HNO_3$	7.32×10^{10}	0.49	17492
R2	$NH_2OH+HNO_3$ → HAN	1.00×10^{12}	0	0
R3	HAN → $NH_3OH^+ + NO_3^-$	1.24×10^{14}	0.08	10862
R4	$NH_3OH^+ + NO_3^-$ → HAN	1.00×10^{12}	0	0
R5	$NH_2OH+HNO_3 \rightleftharpoons NH_2(O)NO_2+H_2O$	1.57	2.78	25067
R6	$NH_2(O)NO_2 \rightleftharpoons HONO+HNO$	5.40×10^{11}	0.71	11324
R7	$NH_3OH^+ + HNO_3 \rightleftharpoons NH_2(OH)NO_2^+ + H_2O$	4.65×10^{1}	3.81	20243
R8	$NH_2(OH)NO_2^+ + NO_3^- \rightleftharpoons NH(OH)NO_2+HNO_3$	1.00×10^{12}	0	0
R9	$NH_2(OH)NO_2^+ + NH_3 \rightleftharpoons NH(OH)NO_2+NH_4^+$	1.00×10^{12}	0	0
R10	$NH_2(OH)NO_2^+ + NH_2OH \rightleftharpoons NH(OH)NO_2+NH_3OH^+$	1.00×10^{12}	0	0
R11	$NH(OH)NO_2 \rightleftharpoons NHOH\cdot + NO_2\cdot$	1.95×10^{13}	1.08	36112
R12	$NH(OH)NO_2 \rightleftharpoons NH(O)N(O)OH$	1.49×10^{10}	0.94	15531
R13	$NH(OH)NO_2+H_2O \rightleftharpoons NH(O)N(O)OH+H_2O$	3.05×10^{2}	2.84	10411
R14	$NH(O)N(O)OH \rightleftharpoons HONO+HNO$	1.18×10^{12}	0.51	17598
R15	$NH_2(OH)NO_2^+ + NO_3^- \rightleftharpoons NH_2(O)NO_2+HNO_3$	1.00×10^{12}	0	0
R16	$NH_2(OH)NO_2^+ + NH_3 \rightleftharpoons NH_2(O)NO_2+NH_4^+$	1.00×10^{12}	0	0
R17	$NH_2(OH)NO_2^+ + NH_2OH \rightleftharpoons NH_2(O)NO_2+NH_3OH^+$	1.00×10^{12}	0	0
R18	$NH_3OH^+ + HONO \rightleftharpoons NH_2(OH)NO^+ + H_2O$	8.38	3.81	7412
R19	$NH_2(OH)NO^+ + NO_3^- \rightleftharpoons NH(OH)NO+HNO_3$	1.00×10^{12}	0	0
R20	$NH_2(OH)NO^+ + NH_3 \rightleftharpoons NH(OH)NO+NH_4^+$	1.00×10^{12}	0	0
R21	$NH_2(OH)NO^+ + NH_2OH \rightleftharpoons NH(OH)NO+NH_3OH^+$	1.00×10^{12}	0	0
R22	$NH(OH)NO \rightleftharpoons HNOH\cdot + NO\cdot$	1.47×10^{12}	0.76	33654
R23	$NH(OH)NO+H_2O \rightleftharpoons N_2O+H_2O+H_2O$	2.45×10^{2}	2.88	12636
R24	$NH(OH)NO+HNO_3 \rightleftharpoons N_2O+H_2O+HNO_3$	3.03×10^{-3}	3.69	11182
R25	$NH(OH)NO+NH_3OH^+ \rightleftharpoons N_2O+H_2O+NH_3OH^+$	2.31	3.18	31974
R26	$NH(OH)NO+HONO \rightleftharpoons N_2O+H_2O+HONO$	3.01×10^{-4}	3.94	15331
R27	$NH_2(O)NO \rightleftharpoons NH_2O\cdot + NO\cdot$	5.40×10^{11}	0.71	11324
R28	$NH_2OH+N_2O_5 \rightleftharpoons NH(OH)NO_2+HNO_3$	3.90×10^{1}	2.90	−3035
R29	$NH_3OH^+ + N_2O_5 \rightleftharpoons NH_2(OH)NO_2^+ + HNO_3$	2.06×10^{1}	3.57	7975
R30	$NH_2OH+N_2O_4 \rightleftharpoons NH(OH)NO_2+HNO_2$	9.44	2.94	12990
R31	$NH_2OH+t-N_2O_4 \rightleftharpoons NH(OH)NO+HNO_3$	1.00×10^{12}	0	0
R32	2 HONO $\rightleftharpoons N_2O_3+H_2O$	4.71	3.57	9688
R33	$NH_2OH+N_2O_3 \rightleftharpoons NH(OH)NO+HONO$	4.45×10^{1}	2.85	3362
R34	$NH_3OH^+ + N_2O_3 \rightleftharpoons NH_2(OH)NO^+ + HONO$	3.80×10^{1}	3.91	4547
R35	$N_2O_3 \rightleftharpoons NO\cdot + NO_2\cdot$	2.07×10^{14}	0.46	6416
R36	$NH_2OH+OH\cdot \rightleftharpoons NH_2O\cdot + H_2O$	1.16×10^{4}	2.86	399
R37	$NH_2OH+OH\cdot \rightleftharpoons HNOH\cdot + H_2O$	6.27×10^{5}	2.39	−635
R38	$NH_2OH+NO_2\cdot \rightleftharpoons NH_2O\cdot + HONO$	6.10	3.31	9667
R39	$NH_2OH+NO_2\cdot \rightleftharpoons NH_2O\cdot + HNO_2$	1.25×10^{1}	3.32	12788
R40	$NH_2OH+NO_2\cdot \rightleftharpoons HNOH\cdot + HONO$	1.04×10^{1}	3.37	10893
R41	$NH_2OH+NO_2\cdot \rightleftharpoons HNOH\cdot + HNO_2$	1.36×10^{1}	3.66	3825
R42	$HNOH\cdot + NO_2\cdot \rightleftharpoons HNO+HONO$	2.09×10^{2}	2.86	12122
R43	$HNOH\cdot + NO_2\cdot \rightleftharpoons HNO+HNO_2$	7.45	3.01	6739
R44	$HNOH\cdot + NO\cdot \rightleftharpoons HNO+HNO$	2.11×10^{3}	2.43	24285
R45	$HNO+OH\cdot \rightleftharpoons NO\cdot + H_2O$	2.06×10^{6}	2.36	−1158
R46	$HNO+NO_2\cdot \rightleftharpoons NO\cdot + HONO$	7.40×10^{-3}	4.39	8869
R47	$HNO+NO_2\cdot \rightleftharpoons NO\cdot + HNO_2$	3.37×10^{1}	3.48	11140
R48	$HNO+HNO \rightleftharpoons HN(O)NHO$	1.80×10^{2}	2.88	7901
R49	$HN(O)NHO \rightleftharpoons NH(OH)NO$	5.74×10^{1}	3.46	20867
R50	$HN(O)NHO+H_2O \rightleftharpoons NH(OH)NO+H_2O$	2.06×10^{2}	2.99	1410
R51	$HN(O)NHO+HNO_3 \rightleftharpoons NH(OH)NO+HNO_3$	1.00×10^{12}	0	0
R52	2 HN(O)NHO $\rightleftharpoons$ 2 NH(OH)NO	1.00×10^{12}	0	0
R53	$HNO+NO\cdot \rightleftharpoons ONHNO\cdot$	2.74×10^{4}	2.68	6790

Table 1 (continue)

R54	$ONHNO\cdot \rightleftharpoons ONNOH\cdot$	1.33×10^{12}	0.38	28888
R55	$ONHNO\cdot + H_2O \rightleftharpoons ONNOH\cdot + H_2O$	8.12×10^{3}	2.39	7136
R56	$ONNOH\cdot \rightleftharpoons N_2O + OH\cdot$	2.09×10^{10}	1.08	11033
R57	$NH_2OH + HNO \rightleftharpoons NH_2(O)NHOH$	6.57×10^{-6}	4.41	12112
R58	$NH_2(O)NHOH \rightleftharpoons NHNHO + H_2O$	8.46×10^{11}	0.70	4683
R59	$NHNHO \rightleftharpoons NHNOH$	5.43×10^{10}	0.92	45801
R60	$NHNHO + H_2O \rightleftharpoons NHNOH + H_2O$	1.53×10^{3}	2.52	13243
R61	$NH_3OH^+ + HNO \rightleftharpoons HNO_2 + NH_4^+$	1.58×10^{-2}	4.41	34211
R62	$NH_2O^- + HNO \rightleftharpoons NHNO^- + H_2O$	4.95×10^{1}	2.52	−1486
R63	$NNHO^- \rightleftharpoons N_2 + OH^-$	4.52×10^{9}	1.30	21234
R64	$NNHO^- + H_2O \rightleftharpoons N_2 + OH^- + H_2O$	9.43×10^{1}	2.69	2983
R65	$NHNO^- + NH_3OH^+ \rightleftharpoons N_2 + H_2O + NH_2OH$	1.00×10^{12}	0	0
R66	$NHNO^- + HNO_3 \rightleftharpoons N_2 + H_2O + NO_3^-$	1.00×10^{12}	0	0
R67	$NHNO^- + NH_4^+ \rightleftharpoons N_2 + H_2O + NH_3$	1.00×10^{12}	0	0
R68	$NH_2OH + H_2O \rightleftharpoons NH_3OH^+ + OH^-$	1.00×10^{12}	0	0
R69	$NH_2OH + H_2O \rightleftharpoons NH_2O^- + H_3O^+$	1.00×10^{12}	0	0
R70	$2\,NH_2OH \rightleftharpoons NH_3OH^+ + NH_2O^-$	1.00×10^{12}	0	0
R71	$2\,NH_2OH \rightleftharpoons 2\,NH_3O$	4.19×10^{-1}	3.07	4339
R72	$2\,NH_2OH \rightleftharpoons NH_2NH_2O + H_2O$	4.47×10^{-2}	3.91	29313
R73	$2\,NH_2OH + H_2O \rightleftharpoons NH_2NH_2O + 2H_2O$	1.66×10^{-10}	6.07	25422
R74	$2\,NH_2OH + NH_2OH \rightleftharpoons NH_2NH_2O + H_2O + NH_2OH$	1.10×10^{-11}	5.87	19720
R75	$2\,NH_2OH + NH_3OH^+ \rightleftharpoons NH_2NH_2OH^+ + H_2O + NH_2OH$	9.22×10^{-12}	6.28	13692
R76	$NH_2NH_2OH^+ + NO_3^- \rightleftharpoons NH_2NH_2O + HNO_3$	1.00×10^{12}	0	0
R77	$NH_2NH_2OH^+ + NH_3 \rightleftharpoons NH_2NH_2O + NH_4^+$	1.00×10^{12}	0	0
R78	$NH_2NH_2OH^+ + NH_2OH \rightleftharpoons NH_2NH_2O + NH_3OH^+$	1.00×10^{12}	0	0
R79	$NH_2NH_2O \rightleftharpoons HNO + NH_3$	8.69×10^{-6}	6.01	32958
R80	$NH_2NH_2O + H_2O \rightleftharpoons HNO + NH_3 + H_2O$	5.74×10^{3}	2.39	23459
R81	$NH_2OH + NH_3O \rightleftharpoons NH_2(O)OH + NH_3$	6.57	3.63	34237
R82	$NH_2(O)OH \rightleftharpoons H_2O + HNO$	8.46×10^{11}	0.70	4683
R83	$NH_2OH + NH_2O^- \rightleftharpoons NH_2NHO^- + H_2O$	4.95×10^{-1}	3.46	17620
R84	$NH_2NHO^- + H_2O \rightleftharpoons NH_2NH_2O + OH^-$	1.00×10^{12}	0	0
R85	$NH_2NHO^- + NH_4^+ \rightleftharpoons NH_2NH_2O + NH_3$	1.00×10^{12}	0	0
R86	$NH_2NHO^- + NH_3OH^+ \rightleftharpoons NH_2NH_2O + NH_2OH$	1.00×10^{12}	0	0
R87	$NH_2NHO^- \rightleftharpoons NH_3 + {}^1NO^-$	1.25×10^{13}	0.81	32002
R88	${}^1NO^- + NH_3OH^+ \rightleftharpoons HNO + NH_2OH$	1.00×10^{12}	0	0
R89	${}^1NO^- + H_3O^+ \rightleftharpoons HNO + H_2O$	1.00×10^{12}	0	0
R90	${}^1NO^- + H_2O \rightleftharpoons HNO + OH^-$	1.00×10^{12}	0	0
R91	${}^1NO^- + NH_4^+ \rightleftharpoons HNO + NH_3$	1.00×10^{12}	0	0
R92	$NH_2OH + NO_3^- \rightleftharpoons NH_2O^- + HNO_3$	1.00×10^{12}	0	0

(NO_2^+) and 63 (HNO_3^+). No materials including carbon were employed during the trials, and so no species containing carbon were observed. The gas generation plots in Figure 3 were obtained by summing the intensities of the mass fragments of the different gases, as explained below. These data show that the thermal decomposition of aqueous HAN produces primarily H_2O, N_2O and HNO_3, with a minor amount of N_2 and NH_3. (It is noted that difference of ionization efficiency was not considered in this study.) These major species are in good agreement with the computational predictions.

In the EI MS mode, molecules are broken into smaller fragments by electrons and so, to obtain the true intensities of the various gases, the outputs of the various fragments must be summed, while subtracting overlapping unrelated peaks. As an example, the peak at m/z 30 (corresponding to NO^+) is due to the contributions of fragments from NO, HNO_3, N_2O and NO_2. These calculations were performed based on the known ratios of various mass fragments in a previously published database[41] as well as prior data acquired for HNO_3[42]. The associated equations for each species are presented below as Equations (8) through (15).

$$I^{total}_{HNO_3} \cong I^{63}_{HNO_3^+} + I^{46}_{NO_2^+} + I^{30}_{NO^+(NO_2^+)} = I^{63}_{HNO_3^+} + \frac{10000}{219} I^{63}_{HNO_3^+} + \frac{8570}{219} I^{63}_{HNO_3^+} \quad (8)$$

$$I^{total}_{NO_2} \cong I^{46}_{NO_2^+} + I^{30}_{NO^+(NO_2^+)} - I^{46}_{NO_2^+(HNO_3^+)} = I^{46}_{NO_2^+} - \frac{10000}{219} I^{63}_{HNO_3^+} + \frac{9999}{3703}\left(I^{46}_{NO_2^+} - \frac{10000}{219} I^{63}_{HNO_3^+}\right) \quad (9)$$

Table 2 Calculated thermodynamic data for important species associated with HAN decomposition.

Species	$\Delta_f H^\circ_{liq,calc}$ [kJ mol^{-1}]	$S^\circ_{liq,calc}$ [J mol^{-1}K^{-1}]	C_P [J K^{-1} mol^{-1}]				
			300	400	500	600	800
$[NH_3OH^+][NO_3^-]$	−289.82	359.99	98.67	116.06	131.82	145.23	165.85
NH_2OH	−63.00	243.09	44.7	50.65	56.55	61.76	70.17
HNO_3	−147.27	271.78	53.08	62.71	70.41	76.4	84.75
NH_3OH^+	−12.38	243.26	43.86	51.06	58.87	66.21	78.62
NO_3^-	−183.82	251.39	44.7	52.66	59.22	64.25	70.87
NH_3O	−35.62	227.26	37.8	43.98	50.58	56.68	66.85
NH_2O^-	71.61	228.65	37.63	42.42	47.06	51.1	57.55
HONO	−88.04	247.14	44.02	50.07	54.99	58.9	64.55
HNO_2	−63.33	238.28	38.48	43.86	49.26	54.02	61.36
HNO	100.26	220.59	33.7	34.99	36.9	39.02	43.01
N_2O_5	26.93	359.79	88.65	102.05	112.48	120.52	131.47
N_2O_4	19.37	323.22	73.28	83.87	92.32	99.05	108.53
trans-$ONONO_2$	32.35	336.78	81.81	91.86	99.79	105.96	114.53
N_2O_3	86.47	304.98	69.09	75.9	81.45	86.01	92.7
$NO_2\cdot$	43.94	239.91	37	40.08	43.07	45.69	49.58
NO_2^-	−81.02	236.85	37.17	40.89	44.3	47.07	50.87
N_2O	82.12	219.36	38.01	41.99	45.14	47.72	51.63
NO·	97.03	205.16	29.16	29.44	30.01	30.75	32.27
$^1NO^-$	275.24	201.04	29.47	30.31	31.36	32.36	33.92
N_2	−2.76	191.46	29.11	29.2	29.47	29.93	31.15
NH_3	−56.51	198.13	34.77	37.35	40.45	43.59	49.47
NH_4^+	−93.96	191.59	34.87	38.7	43.77	49.04	58.77
H_2O	−270.6	188.77	33.47	34.1	35.03	36.09	38.36
H_3O^+	−185.94	207.81	35.2	37.89	40.95	43.96	49.5
OH^-	−142.86	172.23	29.1	29.1	29.12	29.19	29.57
OH·	15.06	178.19	29.1	29.1	29.12	29.19	29.58
$NH_2(O)OH$	−91.49	266.94	53.96	63.02	71.47	78.73	90.05
NH_2NH_2O	45.89	265.82	54.23	65.7	76.58	86.03	100.96
$NH_2NH_2OH^+$	38.31	275.44	62.01	74.72	86.83	97.4	114.23
NH_2NHO^-	137.78	263.22	53.36	63.55	72.49	79.91	91.26
$NH_2(O)NO_2$	34.53	309.69	74.11	85.82	96.25	105	118.12
$NH(OH)NO_2$	−36.53	298.7	73.09	86.71	97.88	106.73	119.35
$NH_2(OH)NO_2^+$	81.24	326.7	75.14	89.29	101.57	111.76	127.08
$NH_2(O)NO$	138.39	294.24	65.33	74.01	81.88	88.56	98.8
NH(OH)NO	45.52	285.63	65.73	75.26	83.4	90.06	99.86
$NH_2(OH)NO^+$	137.15	317.1	70	80.07	88.89	96.37	108.09
NH(O)N(O)OH	25.51	295.5	74.04	88.05	99.16	107.9	120.42
$NH_2(O)NHOH$	11.05	285.41	65.57	80.76	94.3	105.59	122.74
NH(O)NHO	45.57	263.39	57.59	68.24	77.6	85.34	96.87
NHNHO	92.3	251.57	42.08	50.09	57.7	64.24	74.3
NHNOH	55.59	254.34	46.75	55.1	62.27	68.13	76.85
$NNHO^-$	198.81	250.03	40.13	46.09	51.57	56.21	63.21
$NH_2O\cdot$	33.19	225.46	34.64	37.33	40.57	43.73	49.23
HNOH·	76.15	233.21	38.24	42.97	47.45	51.29	57.33
$NH_2\cdot$	171.41	194.68	33.57	34.34	35.42	36.64	39.28

$$I^{total}_{N_2O} \cong I^{44}_{N_2O^+} + I^{30}_{NO^+(N_2O^+)} + I^{28}_{N_2^+(N_2O^+)} = I^{44}_{N_2O^3} + \frac{3113}{9999} I^{44}_{N_2O^+} + \frac{1008}{9999} I^{44}_{N_2O^3} \quad (10)$$

$$I^{total}_{NO} \cong I^{30}_{NO^+} - I^{30}_{NO^+(N_2O^+)} - I^{30}_{NO^+(NO_2^+)} - I^{30}_{NO^+(HNO_3^+)} = I^{30}_{NO^+} - \frac{3113}{9999} I^{44}_{N_2O)} - \frac{9999}{3703}\left(I^{46}_{NO_2^+} - \frac{10000}{219} I^{63}_{HNO_3^+}\right) - \frac{8570}{219} I^{63}_{HNO_3^+} \quad (11)$$

$$I^{total}_{NH_2OH} \cong I^{33}_{NH_2OH^+} \quad (12)$$

$$I^{total}_{N_2} \cong I^{28}_{N_2^+} - I^{28}_{N_2^+(N_2O^+)} + \frac{1}{2} I^{14}_{OH^+} = I^{28}_{N_2^+} - \frac{1008}{9999} I^{44}_{N_2O^+} + \frac{1}{2}\frac{1379}{9999}\left(I^{28}_{N_2^+} - \frac{1008}{9999} I^{44}_{N_2O^+}\right) \quad (13)$$

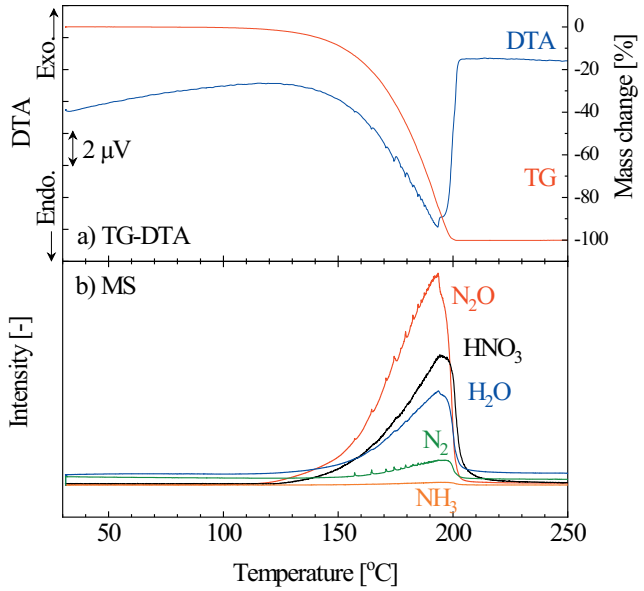

Figure 3 TG-DTA-MS results obtained from an aqueous HAN solution (92 wt%) at a heating rate of 10 °C min^{-1}.

$$I_{H_2O}^{total} \cong I_{H_2O^+}^{18} + I_{OH^+(H_2O^+)}^{17} = I_{H_2O^+}^{18} + \frac{2122}{9999} I_{H_2O^+}^{18} \tag{14}$$

$$I_{NH_3}^{total} \cong I_{NH_3^+}^{17} - I_{OH^+(H_2O^+)}^{17} + I_{NH_2^+(NH_3^+)}^{16} = I_{NH_3^+}^{17} - \frac{2112}{9999} I_{H_2O^+}^{18} + \frac{8007}{9999}\left(I_{NH_3^+}^{17} - \frac{2112}{9999} I_{H_2O^+}^{18}\right) \tag{15}$$

Here, $I_{i(f)}^{n}$ is the relative intensity of ionized gas or ion fragment i, having $m/z = n$ and related to species f. Using these equations, the relative intensity plots in Figure 3 were obtained from the original MS data.

From these two validation studies, it was concluded that the YNU-L 3.0 model provides accurate predictions of the thermal decomposition of aqueous HAN. Despite this, the model could be improved with respect to various points. In future work, the new model should include physical changes to improve the simulation of HAN decomposition. The model, currently, does not include physical changes, evaporation and gasification, so the model cannot consider gas-phase reactions of which dominant mechanism is radical pathways that generates more N_2 gas[27]. The lack of physical changes affects accuracy of heat flow curve and product species. Models including gas-phase reaction will be able to reproduce N_2 generation as detected in TG-DTA-MS study. In addition to this, it should incorporate additional solvation effects so as to accurately assess entropy effects on the rotation and translation of molecules in liquid. Thermochemical data essentially affects accuracy of reaction simulations, so heat of reaction and onset temperature may be drastically changed.

A possible decomposition mechanism was constructed based on the rate of production (ROP) data generated using the YNU-L 3.0 model. Figure 4 shows the ROP results for the important species NH_3OH^+, HNO_3, HONO and HNO during exothermic decomposition. These data indicate the elementary reactions that play important roles in the production or reduction of each species. Figures 4(a) and 4(b) demonstrate that NH_3OH^+ decreases via the reaction $NH_3OH^+ + HNO_3 \rightarrow NH_2(OH)NO_2^+ + H_2O$ and $NH_3OH^+ + HONO \rightarrow NH_2(OH)NO^+ + H_2O$. The decomposition begins with the onset of the former reaction at approximately 155 °C, after which the latter follows and eventually becomes dominant. The products of the former reaction decompose to HNO and HONO via the reactions $NH_2(OH)NO_2^+ + NO_3^- \rightarrow NH_2(O)NO_2 + HNO_3$ and $NH_2(O)NO_2 \rightarrow HNO + HONO$. The resulting HONO immediately reacts with NH_3OH^+ to give the latter reaction, as shown in Figure 4(c). These reactions, the products of which function as catalysts for subsequent reactions, are typical of an auto-catalytic mechanism. In Figure 2, the HONO concentration is seen to remain at almost zero concentration during the entire process, suggesting that HONO maintains a low steady-state level. Products from the latter reaction given above decompose to N_2O and H_2O via the reactions $NH_2(OH)NO^+ + NO_3^- \rightarrow NH(OH)NO + HNO_3$ and $NH(OH)NO + H_2O \rightarrow N_2O + 2H_2O$. These processes regenerate HNO_3 in an exothermic manner[26], thus promoting the initial decomposition (HNO_3-NH_3OH^+ mechanism), as shown in Figure 4(b). Subsequently, the reaction cycle repeats to accelerate the thermal decomposition of the HAN. This reaction scheme can be summarized as follows (here, the reaction numbers correspond to those in Table 1).

Scheme 1. HNO_3-NH_3OH^+ mechanism

$HAN \rightarrow NH_3OH^+ + NO_3^-$	(R1)
$NH_3OH^+ + HNO_3 \rightarrow NH_2(OH)NO_2^+ + H_2O$	(R7)
$NH_2(OH)NO_2^+ + NO_3^- \rightarrow NH_2(O)NO_2 + HNO_3$	(R15)
$NH_2(O)NO_2 \rightarrow HNO + HONO$	(R6)

(overall) $HAN \rightarrow HNO + HONO + H_2O$

Scheme 2. HONO-NH_3OH^+ mechanism

$HAN \rightarrow NH_3OH^+ + NO_3^-$	(R1)
$NH_3OH^+ + HONO \rightarrow NH_2(OH)NO^+ + H_2O$	(R18)
$NH_2(OH)NO^+ + NO_3^- \rightarrow NH(OH)NO + HNO_3$	(R19)
$NH(OH)NO + H_2O \rightarrow N_2O + H_2O + H_2O$	(R23)

(overall) $HAN + HONO \rightarrow N_2O + 2H_2O + HNO_3$

Figure 4(d) summarizes the ROP data for HNO, which is the other product from the HNO_3-NH_3OH^+ decomposition path. Following the initial decomposition, the HNO transitions to the dimer NH(O)NHO, which then decomposes to N_2O and H_2O via NH(OH)NO. This scheme can be written as follows.

Scheme 3. HNO decomposition mechanism

$HNO + HNO \rightarrow NH(O)NHO$	(R4)
$NH(O)NHO + H_2O \rightarrow NH(OH)NO + H_2O$	(R50)
$NH(OH)NO + H_2O \rightarrow N_2O + H_2O + H_2O$	(R23)

(overall) $2HNO \rightarrow N_2O + H_2O$

These three schemes can be summarized to provide an overall mechanism for the thermal decomposition of aqueous HAN in one single chemical equation as shown in

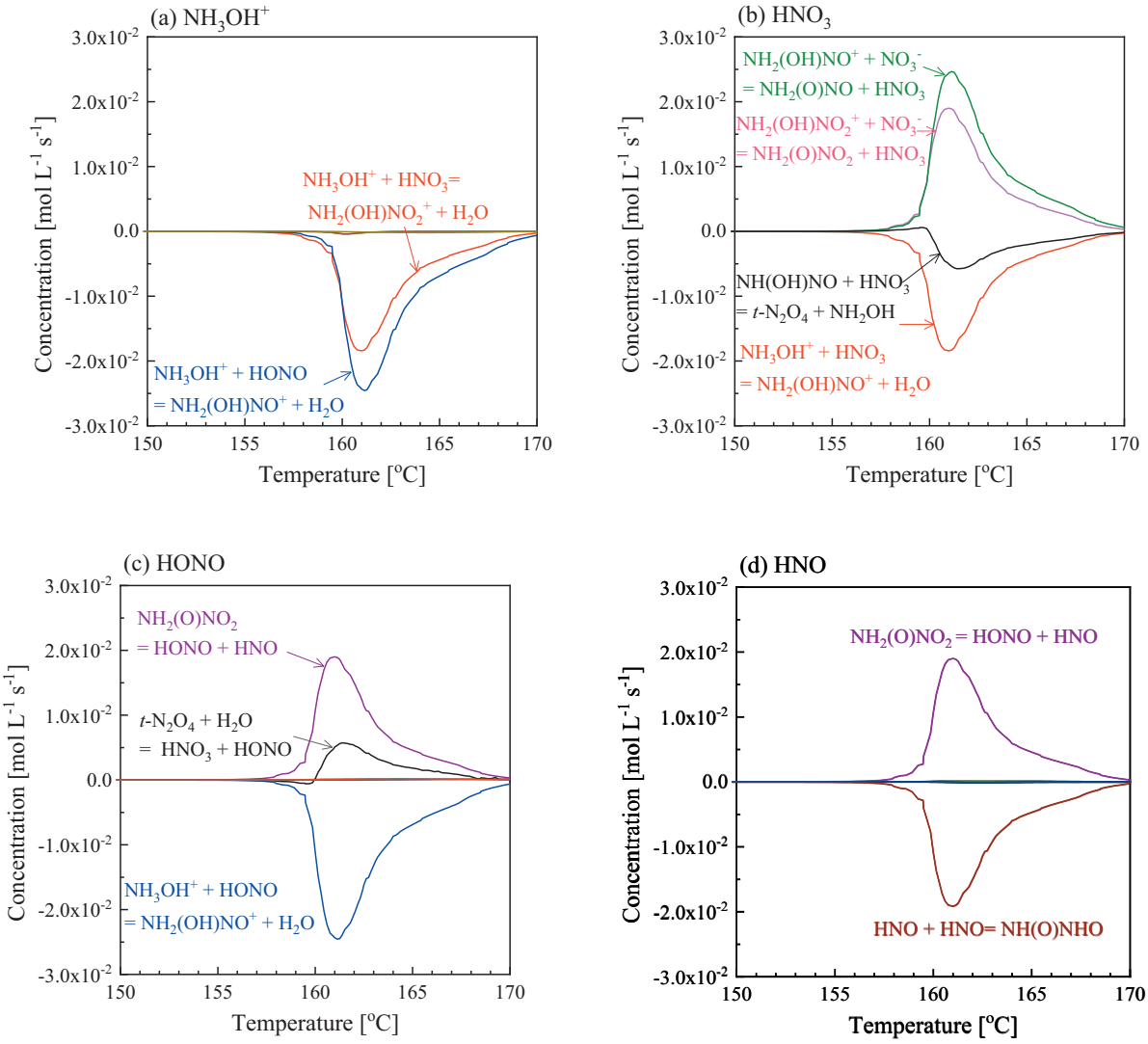

Figure 4 ROP data for important species during HAN decomposition: (a) NH_3OH^+, (b) HNO_3, (c) HONO, and (d) HNO.

Scheme 4. The same equation is obtained by the simulated product ratios in Figure 2, and the validity of simulated products is supported by the TG-DTA-MS study.

Scheme 4. Thermal decomposition of aqueous HAN

$HAN \rightarrow HNO + HONO + H_2O$ (Scheme 1)

$HAN + HONO \rightarrow N_2O + 2\,H_2O + HNO_3$ (Scheme 2)

$HNO \rightarrow 0.5\,N_2O + 0.5\,H_2O$ (Scheme 3)

(overall) $HAN \rightarrow 0.75\,N_2O + 1.75\,H_2O + 0.5\,HNO_3$

4. Conclusions

A detailed chemical kinetics model (YNU-L 3.0) was developed for aqueous HAN decomposition in the liquid phase. The associated mechanisms were identified and assessed by quantum chemistry calculations using the G4//ωB97X-D/6-311++G(d,p)/SCRF=(smd, solvent=water) level of theory. Rate coefficients were calculated that allowed TST and VTST analyses of the reactions, and the rate coefficients for radical recombination reactions and proton transfers with no energy barriers were set to the diffusion limited value of 10^{12} cm^3 mol^{-1} s^{-1}. Thermal corrections, entropy and heat capacityvalues were then calculated from the partition functions using statistical mechanics. The heats of formation for gas and liquid phase molecules were determined by the traditional atomization method combined with the G4 and G4/SCRF=(smd, solvent=water) levels of theory.

The YNU-L 3.0 model consists of 167 reactions and 63 species and this model successfully predicted the thermal decomposition of a 92 wt% HAN solution in water at a heating rate of 1 °C min^{-1}. The predicted thermal properties ($T_{onset,sim.}$ = 151 °C, $T_{top,sim.}$ = 157 °C, $Q_{exo.,sim.}$ = 1.5 kJ g^{-1}) were in good agreement with the experimental data ($T_{onset,C80}$ = 149 °C, $T_{top,C80}$ = 151 °C, $Q_{exo.,C80}$ = 1.6 kJ g^{-1}). The model also calculated the evolved gases and the results were reasonably accurate compared to experimental observations using TG-DTA-MS. Based on these outcomes, we consider that the YNU-L 3.0 model has been validated. However, in future work, the model should be improved to include physical changes and more suitable solvation effects.

This YNU-L 3.0 model allowed the construction of a detailed decomposition mechanism based on first principles. In this mechanism, the initial reaction $HAN \rightarrow HNO + HONO + H_2O$ triggers the overall decomposition, while the subsequent exothermic reactions $HAN + HONO \rightarrow N_2O + 2H_2O + HNO_3$ and $2HNO \rightarrow N_2O + H_2O$ accelerate

the decomposition. These processes can be combined into a single reaction equation: HAN → 0.75 N_2O+1.75 H_2O+0.5 HNO_3.

In the future, the YNU-L 3.0 model should be improved in various aspects. Our model needs more experimental validations. We are also seeking for not only a precise but also theoretically-supported solvation-model to evaluate the entropy of species in solutions.

Acknowledgement

This research was supported by the Foundation for the Promotion of Industrial Explosives Technology 2018 and JSPS KAKENHI Grant Number 17H00844.

References

1) A. B. Fukuchi, S. Nagase, H. Maruizumi, and M. Ayabe, IHI Engineering Review, 43, 22–28 (2010).
2) T. Katsumi, H. Kodama, T. Matsuo, H. Ogawa, N. Tsuboi, and K. Hori, Combust. Explos. Shock Waves, 45, 442–453 (2009).
3) B. N. Kondrikov, V. Annikov, Y. Egorshev, and L. T. Luca, Combust. Explos. Shock Waves, 36, 135–145 (2000).
4) T. Katsumi, H. Kodama, H. Ogawa, N. Tsuboi, and K. Hori, Sci. Tech. Energetic Materials, 70, 27–32 (2009).
5) T. Katsumi, T. Inoue, J. Nakatsuka, K. Hasegawa, K. Kobayashi, S. Sawai, and K. Hori, Combust. Explos. Shock Waves, 48, 536–543 (2012).
6) T. W. Hawkins, A. J. Brand, M. B. McKay, and M. Tinnirello, Proc. the 4th IAASS Conference, 19–21, International Association for the Advancement of Space Safety, Huntsville (2010).
7) Y. P. Chang and K. K. Kuo, Proc. AIAA/ASME/SAE/ASEE joint Propulsion Conf. and Exibit, AIAA Paper 2001–3272, American Institute of Aeronautics and Astronautics, Salt Lake City (2001).
8) D. G. Harlow, R. E. Felt, S. Agnew, G. S. Barney, J. M. McKibben, R. Garber, and M. Lewis, Technical Report on Hydroxylamine Nitrate, U. S. Department of Energy (1998).
9) C. Wei, W. J. Rogers, and M. S. Mannan, J. Hazard. Mater., 130, 163–168 (2006).
10) P. Thakre, Y. Duan, and V. Yang, Combust. Flame, 161, 347–362 (2014).
11) N. E. Ermolin, Combust. Explos. Shock Waves, 40, 92–106 (2004).
12) J. Park, D. Chakraborty, and M. C. Lin, Symp. (int.) Combust. 27, 2351–2357 (1998).
13) N. Kumbhakarna and S.T. Thynell, Thermochim. Acta, 582, 25–34 (2014).
14) R. W. Ashcraft, S. Raman, and W. H. Green, J. Phys. Chem. A, 112, 7577–7593 (2008).
15) A. Sankaranarayanan, L. Mallick, and N. R. Kumbhakarna, J. Therm. Anal. Calorim., 131, 427–441 (2018).
16) Y. Izato and A. Miyake, Combust. Flame, 113, 1475–1480 (2018).
17) Y. Izato, M. Koshi, and A. Miyake, Sci. Tech. Energetic Materials, 78, 12–18 (2017).
18) Y. Izato and A. Miyake, Sci. Tech. Energetic Materials, 78, 143–149 (2017).
19) Y. Izato and A. Miyake, Sci. Tech. Energetic Materials, 79, 166–174 (2018).
20) H. Lee and T. A. Litzinger, Combust. Flame, 135, 151–169 (2003).
21) J. C. Oxley and K. R. Brower, Proc. SPIE 0872, 63–69, Int. Soc. Opt. Eng., Los Angeles (1988).
22) N. Klein, Proc. 27th JANNAF combustion subcommittee meeting, 443–450, International Propulsion Committee, Cheyenne (1990).
23) P. Khare, V. Yang, H. Meng, G. A. Risha, and R. A. Yetter, Combust. Sci. Technol., 187, 1065–1078 (2015).
24) P. Khare, Decomposition and ignition of HAN-based monopropellants by electrolysis. M.S. thesis, Pennsylvania State University (2009).
25) K. Zhang and S. T. Thynell, J. Phys. Chem. A., 122, 8086–8100 (2018).
26) Y. Izato, M. Koshi, and A. Miyake. Cent. Eur. J. Energ. Mater., 14, 888–916 (2017).
27) Y. Izato and A. Miyake, Sci. Tech. Energetic Materials, 79, 108–114 (2018).
28) Y. Izato, M. Koshi, and A. Miyake, Int. J. Chem. Kinet., 49, 83–89 (2017).
29) Y. Izato and A. Miyake, J. Therm. Anal. Calorim., 134, 813–814 (2018).
30) J. D. Chai and M. Head–Gordon, Phys. Chem. Chem. Phys., 10, 6615–6620 (2008).
31) M. J. Frisch, G. W. Trucks, H. B. Schlegel, G. E. Scuseria, M. A. Robb, J. R. Cheeseman, G. Scalmani, V. Barone, B. Mennucci, G. A. Petersson, H. Nakatsuji, M. Caricato, X. Li, H. P. Hratchian, A. F. Izmaylov, J. Bloino, G. Zheng, J. L. Sonnenberg, M. Hada, M. Ehara, K. Toyota, R. Fukuda, J. Hasegawa, M. Ishida, T. Nakajima, Y. Honda, O. Kitao, H. Nakai, T. Vreven, J. A. Montgomery, J. E. Peralta, F. Ogliaro, M. Bearpark, J. J. Heyd, E. Brothers, K. N. Kudin, V. N. Staroverov, T. Keith, R. Kobayashi, J. Normand, K. Raghavachari, A. Rendell, J. C. Burant, S. S. Iyengar, J. Tomasi, M. Cossi, N. Rega, J. M. Millam, M. Klene, J. E. Knox, J. B. Cross, V. Bakken, C. Adamo, J. Jaramillo, R. Gomperts, R. E. Stratmann, O. Yazyev, A. J. Austin, R. Cammi, C. Pomelli, J. W. Ochterski, R. L. Martin, K. Morokuma, V. G. Zakrzewski, G. A. Voth, P. Salvador, J. J. Dannenberg, S. Dapprich, A. D. Daniels, O. Farkas, J. B. Foresman, J. V. Ortiz, J. Cioslowski, and D. J. Fox, Gaussian 09, Revision D.01, Gaussian, Inc., Wallingford CT (2010).
32) L. A. Curtiss, P. C. Redfern, and K. Raghavachari, J. Chem. Phys., 126, 1–12 (2007).
33) V. S. Bernales, A. V. Marenich, R. Contreras, C. J. Cramer, and D. G. Truhlar, J. Phys. Chem. B, 116, 9122–9129 (2012).
34) A. Miyoshi, GPOP software, rev. 2013.07.15 m7, available from the author. See http://akrmys.com/gpop/. (accessed 18-June-2018). (online).
35) J. I. Steinfeld, J. S. Francisco, and W. L. Hase, "Chemical Kinetics and Dynamics, 2nd ed.", Prentice Hall (1998).
36) J. W. Ochterski, Thermochemistry in Gaussian, Gaussian, Inc., Wallingford CT (2000), http://www.lct.jussieu.fr/manuels / Gaussian 03 / g _ whitepap / thermo / thermo. pdf. (accessed 18-June-2018). (online).
37) T. R. Tuttle, S. Malaxos, and J. V. J. Coe, J. Phys. Chem. A, 106, 925–932 (2002).
38) W. C. Gardiner Ed., "Thermochemical Data for Combustion Calculations", Springer-Verlag, New York (1984).
39) ANSYS CHEMKIN-PRO 17.1, ANSYS, San Diego (2016).
40) R. A. Sasse', M. A. Davies, R. A. Fifer, M. M. Decker, and A. J. Kotlar, Memorandum Report BRL-MR-3720, U.S. Army Ballistic Research Laboratory (1988).
41) P. J. Linstrom and W. G. Mallard, NIST Chemistry WebBook. NIST Standard Reference Database Number 69. Eds. National Institute of Standards and Technology. http://webbook.nist.gov, (accessed 18-June-2018). (online).
42) R. A. Friedel, J. L. Shultz, and A. G. Sharkey, Anal. Chem., 45, 1128 (1967).